PHYSICAL REVIEW D **89,** 085001 (2014)

Pair production in rotating electric fields

Alexander Blinne[*] and Holger Gies[†]

Theoretisch-Physikalisches Institut, Abbe Center of Photonics, Friedrich-Schiller-Universität Jena, Max-Wien-Platz 1, D-07743 Jena, Germany and Helmholtz-Institut Jena, Fröbelstieg 3, D-07743 Jena, Germany

(Received 22 November 2013; published 31 March 2014)

We explore Schwinger pair production in rotating time-dependent electric fields using the real-time Dirac-Heisenberg-Wigner formalism. We determine the time evolution of the Wigner function as well as asymptotic particle distributions neglecting backreactions on the electric field. Whereas qualitative features can be understood in terms of effective Keldysh parameters, the field rotation leaves characteristic imprints in the momentum distribution that can be interpreted in terms of interference and multiphoton effects. These phenomena may seed characteristic features of QED cascades created in the antinodes of a high-intensity standing wave laser field.

DOI: 10.1103/PhysRevD.89.085001 PACS numbers: 12.20.Ds, 11.15.Tk

I. INTRODUCTION

Schwinger pair production—or the spontaneous decay of the QED vacuum in electric fields—is one of the rare quantum field theory phenomena which is inherently nonperturbative but analytically well understood. Unfortunately, any attempt at verifying this understanding in macroscopic electric fields is hampered by the exponentially small production rate $\sim \exp[-\pi m^2/(eE)]$, where m is the electron mass being huge for typical laboratory field strengths E [1–3]. The rapid development of optical or x-ray high-intensity lasers has lead to many suggestions for schemes for a first discovery [4–14], also including the combination of lasers and strong Coulomb fields [15–18].

However, while the highest field intensities in such systems may indeed gradually approach the critical intensity, $I_{\rm cr} = E_{\rm cr}^2 = (\frac{m^2}{e})^2 \simeq 4.3 \times 10^{29}$ W/cm^2, further possible physical processes may set in that could partly or entirely swamp a pair production signal. In particular QED cascades of successive radiation of accelerated charges and particle production from hard photons are expected to occur [19–28], which may even fundamentally inhibit the generation of near critical intensities.

In view of a possible discovery of Schwinger pair production in strong laser fields, this gives rise to a crucial question: can a QED cascade seeded by an electron (sourced by impurities of an imperfect vacuum) be distinguished from a QED cascade seeded by Schwinger pair production? Whereas the ensemble of electrons arising from impurities are likely to have an isotropic initial momentum distribution, the ensemble of Schwinger created pairs can be expected to carry information about the directionality of the electric field that lead to pair creation.

To quantify this difference for final observables, not only the QED cascade has to be computed, but first of all, the initial data from Schwinger pair production has to be determined. For the cascade calculations performed so far, this is far from being trivial as spatiotemporal dependencies of the fields have to be accounted for. The simplest field model often considered for cascade calculations is a uniformly rotating homogeneous electric field. Such fields serve as a model for the regions of highest electric field strength in the antinodes of a circularly polarized standing wave mode, where QED cascades are expected to occur predominantly. By contrast, first-principles quantum field theory methods for Schwinger pair production typically allow for the treatment of constant unidirectional fields [2,3] with one-dimensional dependencies on either space [29–32] or time [32–40]. More involved fields soon lead to an enormous increase in computational complexity [7,41–43].

In the present work, we consider for the first time Schwinger pair production in a time-dependent rotating spatially homogeneous electric field, that may help bringing the quantum field theory studies a substantial step closer to QED cascade calculations. For this, we use the real-time off-equilibrium Dirac-Heisenberg-Wigner (DHW) (or simply Wigner) formalism on a mean-field level (neglecting backreactions on the electromagnetic field) as developed in [44]. We demonstrate that the coupled partial differential equations (PDE) for the components of the Wigner function can be mapped onto simpler (modified) quantum kinetic equations, as first shown for unidirectional fields in [45,46]. This resemblance to quantum kinetic theory [5,47–51] allows the use of the method of characteristics to solve the PDE with conventional high-precision algorithms.

This technique gives access to the real-time evolution of the distribution functions and physical observables such as the asymptotic pair distributions in momentum space and the total particle yield. We find that the qualitative features of the latter can be interpreted within semiclassical pictures

[*]alexander.blinne@uni-jena.de
[†]holger.gies@uni-jena.de

of pair production (inspired by atomic ionization) [31,33,35] using an effective Keldysh parameter that accounts for the time scales in the problem. By contrast, the momentum distribution is strongly influenced by the field rotation, giving rise to structures that can be interpreted in terms of quantum interferences [12,52–54] and multiphoton processes. We believe that these characteristic structures can serve as a seed for a QED cascade, potentially leaving its imprints in the successive complex many-body dynamics. If so, Schwinger pair production should be well distinguishable from more conventionally sourced QED cascades in rotating electric fields.

This work is organized as follows: Section II briefly summarizes the DHW formalism as it is needed for the main part of the paper. In Sec. III the equations of motion for the Wigner function are adapted to spatially homogeneous, but time-dependent electric fields of arbitrary directionality. This leads to a set of quantum kinetic equations generalizing those previously studied in the literature to the case of arbitrary time-dependent field directions. Our quantitative results for a rotating field are presented in detail in Sec. IV. Conclusions are drawn in Sec. V. Some useful details of the numerical implementation are deferred to the Appendix.

II. THE WIGNER FUNCTION

The DHW formalism for Schwinger pair production has first been presented in [44]. Comprehensive summaries for the present context as well as exact solutions for particular electric fields can be found in [45,46]. In the following, we give a brief summary of the formalism as needed for the present work, following the original literature. The starting point is the Wigner operator defined as the Fourier (Wigner) transform of the equal time density operator of two Dirac field operators in the Heisenberg picture,

$$\widehat{\mathcal{W}}_{ab}(t,\vec{x},\vec{p}) \coloneqq -\frac{1}{2}\int d\vec{s}\, e^{-\frac{i}{\hbar}\vec{p}\cdot\vec{s}} e^{-ie\int_{\vec{x}-\vec{s}/2}^{\vec{x}+\vec{s}/2}\vec{A}(t,\vec{x}')\cdot d\vec{x}'} \times\left[\hat{\Psi}_a\left(t,\vec{x}+\frac{\vec{s}}{2}\right),\hat{\bar{\Psi}}_b\left(t,\vec{x}-\frac{\vec{s}}{2}\right)\right], \quad (1)$$

where the Wilson line operator accounts for gauge invariance. Here $\vec{x}$ is a center-of-mass coordinate of the underlying two-point correlator, and $\vec{s}$ denotes a relative coordinate the Fourier conjugate of which defines the kinetic momentum $\vec{p}$. Replacing the gauge field operator by an external classical field (corresponding to a mean-field or Hartree approximation), the vacuum expectation value of the Wigner operator can be taken which defines the Wigner function $\mathcal{W}$. Using the equations of motion for the fermionic Heisenberg operators, the dynamical equation for the Wigner function can be written as

$$D_t\mathcal{W} = -\frac{1}{2}\vec{D}_{\vec{x}}[\gamma^0\vec{\gamma},\mathcal{W}] - im[\gamma^0,\mathcal{W}] - i\vec{P}\{\gamma^0\vec{\gamma},\mathcal{W}\} \quad (2)$$

with the pseudodifferential operators

$$D_t = \partial_t + e\int_{-1/2}^{1/2} d\lambda \vec{E}(t,\vec{x}+i\lambda\vec{\nabla}_{\vec{p}})\cdot\vec{\nabla}_{\vec{p}},$$
$$\vec{D}_{\vec{x}} = \vec{\nabla}_{\vec{x}} + e\int_{-1/2}^{1/2} d\lambda \vec{B}(t,\vec{x}+i\lambda\vec{\nabla}_{\vec{p}})\times\vec{\nabla}_{\vec{p}},$$
$$\vec{P} = \vec{p} - ie\int_{-1/2}^{1/2} d\lambda\lambda \vec{B}(t,\vec{x}+i\lambda\vec{\nabla}_{\vec{p}})\times\vec{\nabla}_{\vec{p}}.$$

Here, we have used the conventions $\{\gamma^\mu,\gamma^\nu\} = +2\eta^{\mu\nu} = +2\,\mathrm{diag}(1,-1,-1,-1)$ and worked in temporal gauge $A_0 = 0$. In the language of Feynman diagrams, the mean-field approximation corresponds to neglecting radiative corrections, which is justified by the smallness of the fine-structure constant α. The Wigner function can be decomposed in terms of a complete basis of the Clifford algebra, $(\mathbb{1},\gamma^5,\gamma^\mu,\gamma^\mu\gamma^5,\sigma^{\mu\nu} \coloneqq \frac{i}{2}[\gamma^\mu,\gamma^\nu])$,

$$\mathcal{W} = \frac{1}{4}(\mathbb{1}\mathbb{s} + i\gamma_5\mathbb{p} + \gamma^\mu\mathbb{v}_\mu + \gamma^\mu\gamma_5\mathbb{a}_\mu + \sigma^{\mu\nu}\mathbb{t}_{\mu\nu}), \quad (3)$$

with correspondingly transforming coefficient functions, $\mathbb{s},\mathbb{p},\mathbb{v}_\mu,\mathbb{a}_\mu,\mathbb{t}_{\mu\nu}$. The equation of motion can be decomposed accordingly, yielding

$$\begin{aligned}
\mathbb{1}\colon\ & D_t\mathbb{s} = +2\vec{P}\cdot\vec{\mathbb{t}}^1\\
i\gamma_5\colon\ & D_t\mathbb{p} = -2\vec{P}\cdot\vec{\mathbb{t}}^2 - 2m\mathbb{a}^0\\
\gamma^0\colon\ & D_t\mathbb{v}^0 = -\vec{D}_{\vec{x}}\vec{\mathbb{v}}\\
\gamma^0\gamma_5\colon\ & D_t\mathbb{a}^0 = -\vec{D}_{\vec{x}}\vec{\mathbb{a}} + 2m\mathbb{p}\\
\gamma^i\colon\ & D_t\vec{\mathbb{v}} = -\vec{D}_{\vec{x}}\mathbb{v}^0 - 2\vec{P}\times\vec{\mathbb{a}} - 2m\vec{\mathbb{t}}^1\\
\gamma^i\gamma_5\colon\ & D_t\vec{\mathbb{a}} = -\vec{D}_{\vec{x}}\mathbb{a}^0 - 2\vec{P}\times\vec{\mathbb{v}}\\
\sigma^{0i}\colon\ & D_t\vec{\mathbb{t}}^1 = -\vec{D}_{\vec{x}}\times\vec{\mathbb{t}}^2 - 2\vec{P}\mathbb{s} + 2m\vec{\mathbb{v}}\\
\frac{1}{2}\epsilon_{ijk}\sigma^{jk}\colon\ & D_t\vec{\mathbb{t}}^2 = +\vec{D}_{\vec{x}}\times\vec{\mathbb{t}}^1 + 2\vec{P}\mathbb{p},
\end{aligned} \quad (4)$$

with

$$(\vec{\mathbb{t}}^1)_i \coloneqq \mathbb{t}_{0i} - \mathbb{t}_{i0}, \qquad (\vec{\mathbb{t}}^2)_i \coloneqq \epsilon_i{}^{jk}\mathbb{t}_{jk}.$$

A solution of these equations requires initial conditions. For electromagnetic fields that vanish at asymptotically early times, $t\to-\infty$, initial conditions are given by the vacuum solution,

$$\mathbb{s}_{\mathrm{vac}} = \frac{-2m}{\omega(\vec{p})}, \qquad \vec{\mathbb{v}}_{\mathrm{vac.}} = \frac{-2\vec{p}}{\omega(\vec{p})}, \quad (5)$$

where $\omega(\vec{p}) = \sqrt{m^2+\vec{p}^2}$. The coefficient functions can be viewed as distribution functions in phase space with a pseudo-probabilistic interpretation. A full probabilistic

interpretation in coordinate or momentum space arises upon integrating over momenta or coordinates, respectively.

An important auxiliary quantity is the combination

$$\epsilon(t,\vec{x},\vec{p}) = \vec{p}\cdot\vec{\mathbb{v}}(t,\vec{x},\vec{p}) + m\mathbb{s}(t,\vec{x},\vec{p}), \tag{6}$$

which can be interpreted as a (phase space) energy density of the fermionic fields. The corresponding one-particle distribution function in phase space is given by the difference of this energy density as compared to the vacuum energy density, normalized by the particle pair energies,

$$f(t,\vec{x},\vec{p}) = \frac{1}{2\omega(\vec{p})}(\epsilon(t,\vec{x},\vec{p}) - \epsilon_{\mathrm{vac}}(t,\vec{x},\vec{p})). \tag{7}$$

This distribution function will be of central interest for our investigations. It is important to stress that the principles of quantum field theory guarantee a particle interpretation only at asymptotically large times. For instance, the total number of particles (= number of anti-particles = number of pairs) produced out of the vacuum is given by

$$n = \lim_{t\to\infty}\int d\Gamma f(t,\vec{x},\vec{p}), \tag{8}$$

where $d\Gamma$ denotes the phase space measure.

III. QUANTUM KINETIC EQUATIONS IN HOMOGENEOUS ELECTRIC FIELDS

The Wigner formalism, in principle, can deal with pair production in arbitrary electromagnetic fields. In practice, computational cost inhibits a straightforward numerical integration of the coupled set of partial differential equations, see [43] for a first solution in a space- and time-dependent field in $1+1$ dimensions. This limitation suggests to concentrate on highly symmetric or effectively dimensionally reduced configurations. In fact, in [45,46] it has been shown that the Wigner formalism for unidirectional time-dependent spatially homogeneous electric fields can be mapped onto the simpler formalism provided by quantum kinetic theory which has mostly been used in practical computations. In the following, we will drop the condition of unidirectionality in order to allow for rotating fields. From a technical viewpoint, this leads to a higher complexity of the problem in momentum space, but still allows for a mapping of the Wigner formalism onto a modified quantum kinetic description.

Confining ourselves to spatially homogeneous purely electric fields ($\vec{E} = \vec{E}(t), \vec{B} \equiv 0$), the equation of motion for the Wigner function simplifies [44] to

$$(\partial_t + e\vec{E}(t)\cdot\vec{\nabla}_{\vec{p}})\mathbb{w} = \mathcal{M}\mathbb{w}, \tag{9}$$

with the ten nontrivial Wigner coefficient functions,

$$\mathbb{w} = \begin{pmatrix} \mathbb{s} & \vec{\mathbb{v}}, & \vec{\mathbb{a}}, & \vec{\mathbb{t}}^1 \end{pmatrix}^{\mathsf{T}},$$

$$\text{and} \quad \mathcal{M} = \begin{pmatrix} 0 & 0 & 0 & 2\vec{p}^{\mathsf{T}} \\ 0 & 0 & -2\vec{p}\times & -2m \\ 0 & -2\vec{p}\times & 0 & 0 \\ -2\vec{p} & 2m & 0 & 0 \end{pmatrix}.$$

The coefficient functions $\mathbb{p}$ and $\vec{\mathbb{t}}^2$ vanish in this case. Because of spatial homogeneity, all quantities no longer depend on the space coordinate, but only on time and kinetic momentum, e. g., $\mathbb{w} = \mathbb{w}(t,\vec{p})$.

Writing the vacuum solution $\mathbb{w}_{\mathrm{vac}}$ as

$$\mathbb{w}_{\mathrm{vac}} = (\,\mathbb{s}_{\mathrm{vac}} \quad \vec{\mathbb{v}}_{\mathrm{vac}} \quad \vec{0}, \quad \vec{0}\,)^{\mathsf{T}} = -2\mathbb{e}_1, \tag{10}$$

it can straightforwardly be verified that $\mathbb{e}_1$ is a unit vector in $\mathbb{R}^{10}$ with a standard scalar product, $\mathbb{e}_1\cdot\mathbb{e}_1 = 1$. In the same spirit, the one-particle distribution function as defined in Eq. (7) can be written as

$$f = \frac{1}{2}\mathbb{e}_1\cdot(\mathbb{w} - \mathbb{w}_{\mathrm{vac}}). \tag{11}$$

Now, the PDE system (9) can be converted into an ordinary differential equation (ODE) system by the method of characteristics, cf. [44–46]. Inserting a specific path $\vec{p}\to\vec{\pi}(t)$ into a PDE of the form

$$(\partial_t + b_i(t)\partial_{p_i})g_j(t,\vec{p}) = h_{jk}(t,\vec{p})g_k(t,\vec{p}) \tag{12}$$

and comparing the result to

$$\frac{d}{dt}g_j(t,\vec{\pi}(t)) = [(\partial_t + (\partial_t\pi_i)\partial_{p_i})g_j(t,\vec{p})]_{\vec{p}=\vec{\pi}(t)}, \tag{13}$$

we find

$$b_i(t) = \partial_t\pi_i. \tag{14}$$

This implies that with

$$\vec{\pi}_{\vec{q}}(t) = \int_0^t \vec{b}(t')dt' + \vec{\pi}_0 + \vec{q}, \tag{15}$$

and some arbitrary constant $\vec{\pi}_0$ to be fixed below, we can solve

$$\frac{d}{dt}\tilde{g}_j(t,\vec{q}) = \tilde{h}_{jk}(t,\vec{q})\tilde{g}_k(t,\vec{q}), \tag{16}$$

in order to find the solution to the original equation along the characteristics $\vec{\pi}_{\vec{q}}(t)$ according to $\tilde{g}_j(t,\vec{q}) \equiv g(t,\vec{\pi}_{\vec{q}}(t))$. Note that $\vec{q}$ now is only a parameter and can be freely chosen before solving the equation. For a complete picture

of the solution as a function of t and $\vec{p}$, we have to solve the equation for several values of $\vec{q}$.

With this method, the equation of motion of the Wigner function can be brought to the simple form

$$\dot{\tilde{\mathbb{w}}} = \tilde{\mathcal{M}}\,\tilde{\mathbb{w}}, \tag{17}$$

where the tilde notation indicates as before that the corresponding functions are evaluated along the path $\vec{p} = \vec{\pi}_{\vec{q}}(t)$, and the resulting function is then understood as a function of $\vec{q}$, e.g., $\tilde{\mathbb{w}}(t,\vec{q}) \equiv \mathbb{w}(t,\vec{p} = \vec{\pi}_{\vec{q}}(t))$. For a suitable choice of $\vec{\pi}_0$, the characteristics $\vec{\pi}_{\vec{q}}(t)$ coincide with the classical momentum space paths of electrons in the external field according to

$$\begin{aligned}\vec{\pi}_{\vec{q}}(t) &= e\int_0^t \vec{E}(t')dt' + \vec{\pi}_0 + \vec{q} \\ &= -e\vec{A}(t) + \vec{q},\end{aligned} \tag{18}$$

where we have used the Weyl gauge and set $\vec{\pi}_0 = -e\vec{A}(0)$ in the second line. With this choice, the variable $\vec{q}$ can be interpreted as the canonical momentum whereas $\vec{\pi}_{\vec{q}}(t)$ is the kinetic momentum on a trajectory.

Also the one-particle distribution function $\tilde{f}$ can be considered along the characteristics parametrized by t and $\vec{q}$,

$$\tilde{f} = \frac{1}{2}\tilde{\mathbb{e}}_1 \cdot (\tilde{\mathbb{w}} - \tilde{\mathbb{w}}_{\mathrm{vac}}). \tag{19}$$

With Eq. (17) our original PDE problem is mapped onto an ODE problem which is, in principle, amenable to standard solution methods. Upon insertion of the solution into Eq. (19), we can extract the physical information.

However, in practice, the problem is numerically challenging for the following reason: in a case where only few pairs are created the solution only differs very slightly from the vacuum solution. In order to compute this difference, the numerical solution of Eq. (17) must be determined with a very high precision. This problem is amplified further by the fact that the projection onto the unit vector $\tilde{\mathbb{e}}_1$ also results in the computation of small differences of numerical quantities. Thus a reformulation of the equation of motion is required to obtain better numerical sensitivity for small pair creation rates. For simplicity the tilde symbol is dropped from now on, and all following equations will be considered along the characteristics.

For our reformulation, we decompose the Wigner functions into a component parallel to $\mathbb{e}_1$ and its orthogonal complement. The latter part is parametrized as $\mathcal{T}\mathbb{w}_9$ where $\mathcal{T}$ is a 10×9 matrix chosen such that $\mathbb{e}_1^{\mathsf{T}}\mathcal{T} = \mathbb{o}^{\mathsf{T}}$ (with $\mathbb{o}$ being the zero vector). $\mathcal{T}$ must also be constructed such that a 9×10 matrix $\mathcal{R}$ exists, that satisfies $\mathcal{R}\mathcal{T} = \mathbb{1}_9$. The quantity $\mathbb{w}_9$ denotes an auxiliary 9 component vector. We can now plug the ansatz

$$\mathbb{w} = 2(f-1)\mathbb{e}_1 + \mathcal{T}\mathbb{w}_9, \tag{20}$$

which is clearly compatible with Eq. (19), into the equation of motion. We obtain

$$2\dot{f}\mathbb{e}_1 + 2(f-1)\dot{\mathbb{e}}_1 + \dot{\mathcal{T}}\mathbb{w}_9 + \mathcal{T}\dot{\mathbb{w}}_9 = \mathcal{M}\mathcal{T}\mathbb{w}_9, \tag{21}$$

where we have used that $\mathcal{M}\mathbb{e}_1 \equiv \mathbb{o}$. Evolution equations for f and $\mathbb{w}_9$ can finally be read off by applying $\mathbb{e}_1$ and $\mathcal{R}$, respectively, to both sides of the equation. The resulting equations read

$$\begin{aligned}\dot{f} &= \frac{1}{2}\dot{\mathbb{e}}_1^{\mathsf{T}}\mathcal{T}\mathbb{w}_9 \\ \dot{\mathbb{w}}_9 &= \mathcal{M}_9\mathbb{w}_9 + 2(1-f)\mathcal{R}\dot{\mathbb{e}}_1\end{aligned} \tag{22}$$

with

$$\mathcal{M}_9 = \mathcal{R}(\mathcal{M} - \mathbb{e}_1\dot{\mathbb{e}}_1^{\mathsf{T}})\mathcal{T} + \dot{\mathcal{R}}\mathcal{T}, \tag{23}$$

where $0 = \frac{d}{dt}\mathcal{R}\mathcal{T}$ has been used. In our studies we have chosen

$$\mathcal{T} = \left.\begin{pmatrix} -p_x/m & -p_y/m & -p_z/m & 0 & \cdots & 0 \\ & & \mathbb{1}_9 & & & \end{pmatrix}\right|_{\vec{p}\to\vec{\pi}_{\vec{q}}(t)}, \tag{24}$$

and accordingly

$$\mathcal{R} = (\,\mathbb{o} \quad \mathbb{1}_9\,). \tag{25}$$

With this choice

$$\mathcal{M}_9 = \left.\begin{pmatrix} \mathcal{A} & -2\vec{p}\times & -2m \\ -2\vec{p}\times & 0 & 0 \\ \mathcal{B} & 0 & 0 \end{pmatrix}\right|_{\vec{p}=\vec{\pi}_{\vec{q}}(t)},$$

where $\mathcal{A} = \dfrac{-e}{m^2+\vec{p}^2}\,\vec{p}\cdot\vec{E}^{\mathsf{T}}$,

$$\mathcal{B} = \frac{2}{m}(m^2\mathbb{1}_3 + \vec{p}\cdot\vec{p}^{\mathsf{T}}).$$

The matrix $\mathcal{M}_9$ actually has a three dimensional kernel, indicating a possible redundancy in the Wigner functions for the present case. However, since the kernel is field- and thus time-dependent, it is numerically more convenient to solve the differential Eq. (22) without explicitly projecting out this redundancy. In this form, the differential equations—though still challenging—are accessible to straightforward numerical integration. The initial values for the original equations simply translate into $f = 0$ and $\mathbb{w}_9 = 0$ for $t\to-\infty$. In practice, the numerical integration is not initiated at negative infinity but at some finite value. This corresponds to

a discontinuous switch-on of the electric field, which leads to artificial transient oscillations that subside sufficiently fast for our purposes. This and some further details of the numerical evolution of this set of equations are discussed in Appendix A.

IV. ROTATING ELECTRIC FIELDS

The formalism as developed in the preceding section works for spatially homogeneous, but time-dependent electric fields of arbitrary (time-dependent) directionality. As a specific and important example, we focus on rotating electric fields from now on. More precisely, we consider a field pulse of the form

$$\vec{E}(t) = \frac{E_0}{\cosh^2(\frac{t}{\tau})} \begin{pmatrix} \cos(\Omega t) \\ \sin(\Omega t) \\ 0 \end{pmatrix}, \tag{26}$$

characterized by a maximal field value E_0, an angular rotation frequency Ω and a pulse duration τ. This field configuration can be viewed as a model for the field in an anti-node of a standing wave mode with appropriate circular polarization.

For the discussion, it is useful to introduce the dimensionless parameters

$$\varepsilon = \frac{E_0}{E_{\rm cr}} = \frac{eE_0}{m^2}, \qquad \sigma = \Omega\tau, \tag{27}$$

where ε measures the maximum field strength in units of the critical field, and σ is a measure for the number of full rotation cycles within the pulse duration. The dimensionful parameters will be given in units of the QED scale, i.e., the electron mass scale. For instance, the pulse duration is measured in units of the Compton time $1/m$ in units where $\hbar = c = 1$.

The time evolution of this field is illustrated in Fig. 1. In the limit $\Omega = 0$, the rotating field collapses to a nonrotating Sauter-type field, which is one of the few examples where the Wigner function can be calculated analytically, see, e. g., [45]. Note that a carrier envelope phase ϕ with the replacement $\Omega t \to \Omega t + \phi$ would have no effect, as it can be transformed to zero by a rotation of the coordinate system in the (x, y) plane.

A. Total particle yield

The total number of pairs per unit volume $\mathcal{N}$ can be calculated from the distribution function f by integrating over all momenta at $t \to \infty$, cf. Eq. (8),

$$\mathcal{N} = \int \frac{dq^3}{(2\pi)^3} \lim_{t\to\infty} f(t, q) = \int \frac{dq^3}{(2\pi)^3} f_{\rm lim}(q). \tag{28}$$

In practice, the time integration is stopped at some large but finite time $t_{\rm lim}$. Since the electric field amplitude goes to zero sufficiently fast for large times, also the time derivative of f vanishes rather rapidly. For the numerical accuracy reached in the present work, we have observed that values of $t_{\rm lim}$ of the order of 10τ are sufficient (see Appendix A).

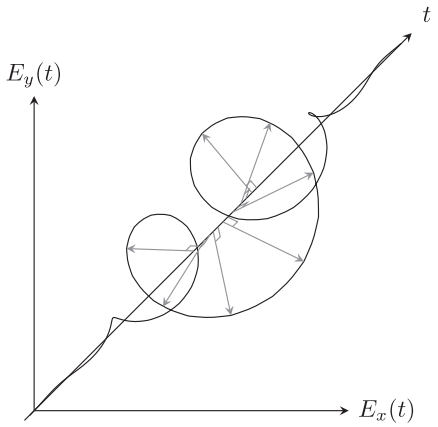

FIG. 1. Illustration of the rotating electric field given in Eq. (26).

As a benchmark, it is useful to compare the particle yield for the known Sauter-type field configuration ($\sigma = 0$) with that generated by rotating fields for different pulse durations and rotation frequencies. A compilation of results for $E_0 = E_{\rm cr}/10$ and for various rotation cycles $\sigma = 0, \ldots, 5$ as a function of the pulse duration is depicted in Fig. 2.

Our results from numerically integrating the Wigner equation (22) for various σ are displayed as symbols. In order to obtain the particle yield $\mathcal{N}$ by integrating over $\vec{q}$, we have chosen a suitable lattice in momentum space $\vec{q}$ and calculated $f(t_{\rm lim}, \vec{q})$ for each lattice point. These results are

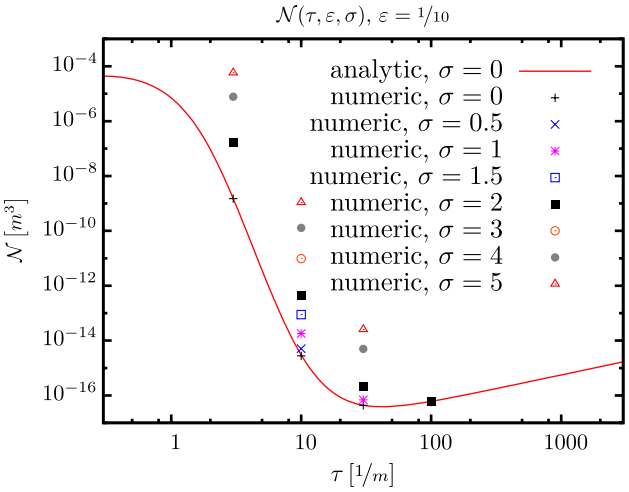

FIG. 2 (color online). Compilation of the total particle yield for a peak field strength $E_0 = \varepsilon E_{\rm cr}$ with $\varepsilon = \frac{1}{10}$ for various rotation cycles σ as a function of the pulse duration τ in units of the Compton time. The solid line marks the analytically soluble case of a nonrotating Sauter pulse with $\sigma = 0$.

compared to the analytically known particle yield for the Sauter pulse for $\sigma = 0$ [45,46] which is shown as a solid red line. As a check, the numerically obtained results for $\sigma = 0$ (black plus symbols) match the analytic curve adequately over several orders of magnitude.

As a main new result, we find that for a given value of pulse duration τ, the particle yield from a rotating pulse can increase several orders of magnitude as compared to the nonrotating case.

This phenomenon can be qualitatively understood in simple terms: let us first recall that the characteristic shape of the particle yield $\mathcal{N}(\tau)$ from the Sauter pulse as displayed by the solid curve in Fig. 2 can be discussed in terms of the Keldysh adiabaticity parameter,

$$\gamma = \frac{1}{\tau\varepsilon m} = \frac{m}{\tau e E_0}. \tag{29}$$

For the Sauter pulse, the value of γ separates the nonperturbative Schwinger regime of pair production ($\gamma \ll 1$) from the perturbative multiphoton regime ($\gamma \gg 1$). In particular, the strong increase in the particle yield for $\tau \lesssim 10$ in Fig. 2 (solid curve) is due to the onset of multiphoton pair production.

Now, switching on the rotation also introduces another time scale $1/\Omega$, such that the Keldysh parameter defined in Eq. (29) is no longer unique, cf. [6]. In particular, in the limit of rapid rotation $\Omega \gg 1/\tau$ we expect the pair production process to be rather characterized by a Keldysh parameter of the form

$$\gamma^\Omega = \frac{\Omega}{\varepsilon m}, \tag{30}$$

since the rotation frequency Ω sets the frequency scale for the photons collectively dominating the rotating pulse.

In this sense, the rapid increase of the particle yield for fixed τ but increasing $\Omega = \sigma/\tau$ visible in Fig. 2 can simply be interpreted as the onset of multiphoton pair production stimulated by the photon components of the field with frequency scale Ω in the spirit of the folding model of [55]. In order to quantify this simple multiphoton picture, we can define a combined Keldysh parameter that interpolates between γ of Eq. (29) and γ^Ω of Eq. (30), for instance,

$$\gamma^* = \frac{\sqrt{1+\sigma^2}}{\tau\varepsilon m}. \tag{31}$$

We emphasize that this is merely a simple choice and by no means unique, other interpolating functions with $\gamma^* \to \gamma$ for $\sigma \to 0$ and $\gamma^* \to \gamma^\Omega$ for $\sigma \to \infty$ may equally well be used.

Figure 3 now shows the same data as Fig. 2 as a function of γ^*. We observe that the data for rotating fields with $\sigma \gtrsim 1$ appears to fall on a universal curve. We conclude that the particle yield no longer depends on σ or τ individually but rather on a combination which is approximately given by

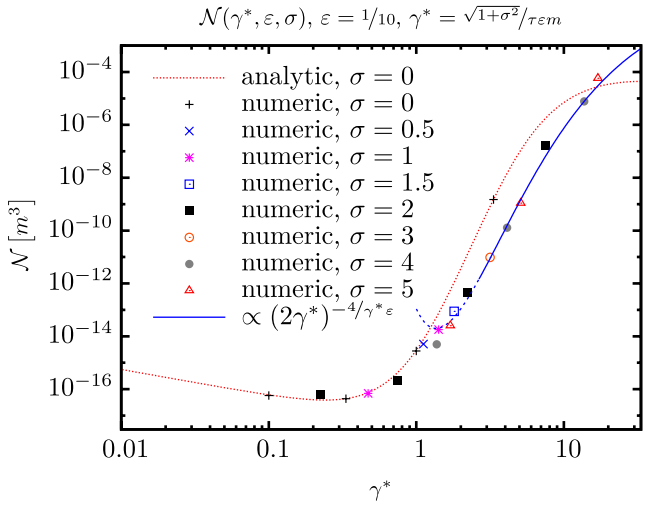

FIG. 3 (color online). Particle yield as a function of γ^* defined in Eq. (31) (same data as in Fig. 2). The blue solid line shows our simple model estimate inspired by a multiphoton picture, matching the data on a universal curve for $\sigma \gtrsim 1$.

our choice of γ^* in Eq. (31). The shape of this universal curve can also be deduced by analogy to the multiphoton regime for linearly polarized oscillations. According to the semiclassical calculations of Refs. [33,35], the multiphoton pair production rate for fields of the form $E(t) = E_0 \cos(\Omega t)$ with $\gamma^\Omega \gg 1$ is given by

$$r \propto \left(\frac{eE_0}{2m\Omega}\right)^{4m/\Omega} = \left(\frac{1}{2\gamma^\Omega}\right)^{4/(\varepsilon\gamma^\Omega)}. \tag{32}$$

Replacing γ^Ω by γ^* and using a fit to this functional dependence on the Keldysh parameter yields the blue solid line in Fig. 3 which satisfactorily matches the data in the multiphoton regime for $\sigma \gtrsim 1$. We conclude that the universal behavior can indeed be interpreted as a multiphoton effect induced by the photons at frequency Ω collectively dominating the rotating electric field.

B. Particle momentum distribution

More information than just the total particle yield is encoded in the one-particle distribution function $f(t, \vec{p})$. In the present section, we first study the physically relevant limit of asymptotic times $t \to t_{\text{lim}}$; more details on the whole time evolution are discussed in the following subsection.

In order to develop an intuition for the rotating case, let us start with the simpler case of a Sauter pulse with $\sigma = 0$, cf. [45,46]. In this case, the distribution depends only on the kinetic momentum p_x parallel to the direction of the electric field and the modulus of the perpendicular momentum $p_\perp = \sqrt{p_y^2 + p_z^2}$. The resulting distribution has a single peak centered at $p_x = \varepsilon\tau$ and $p_\perp = 0$.

An example for a field strength of $\varepsilon = 0.1$ is shown in Fig. 4 in terms of a contour plot in the p_x, p_y plane (which is identical with the $p_x, p_\perp$ plane for $p_z = 0$). The quantitative values of the distribution function are given as the numbers on the contour lines expressed in units given in brackets in the plot title (10^{-12} in this case). The axes ranges are chosen such that the plot is centered about the main features of the distribution while maintaining a square aspect ratio, i. e., the horizontal and vertical axis have the same absolute scale. The contour plot is produced from a smooth interpolating function; the red dots indicate the grid of the numerically calculated data points.

The black cross marks the point where the canonical momentum vanishes $\vec{q} = 0$. For the Sauter pulse, this is equivalent to $\vec{p} = eE_0\tau\vec{e}_x$, cf. Eq. (18), which is the position of the maximum of the peak. This is in agreement with a simple semiclassical picture that particles are predominantly created at rest through instantaneous tunneling around the time when the field has reached its maximum and are afterwards accelerated by the electric field to finite momentum.

Now, let us switch on rotation: for a moderately small number of rotation cycles, $\sigma \sim \mathcal{O}(1)$, we observe that the distribution in momentum space is circularly distorted, see Fig. 5 for $\sigma = 3$. In the semiclassical picture, this can be understood from the fact that the field changes direction during the creation of particles. As a consequence, the particles are accelerated into different directions depending on their instant of creation. In agreement with this simple picture, we also find that the amount of circular distortion depends on the pulse length. For instance, decreasing the pulse duration for fixed rotation frequencies also the circular distortion is weakened, as the created particles have little time to follow the rotating field pulse. We also observe that the peak of the distribution is no longer given by the point of vanishing canonical momentum $\vec{q} = 0$ (black cross in Fig. 5), but at least remains in the vicinity of this point.

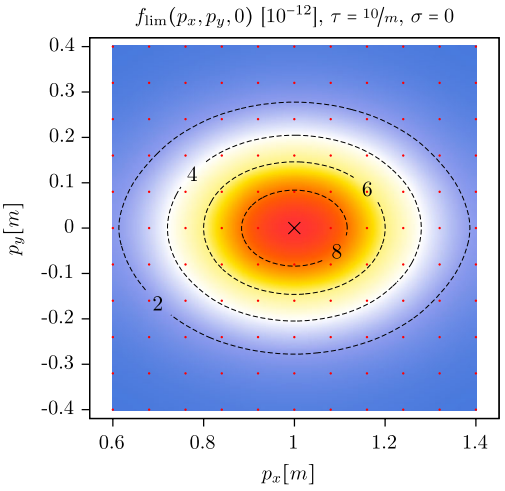

FIG. 4 (color online). Particle momentum distribution created by a Sauter pulse ($\sigma = 0$) with a pulse duration of $\tau = 10/m$ and a peak field strength $\varepsilon = E_0/E_{\mathrm{cr}} = 0.1$.

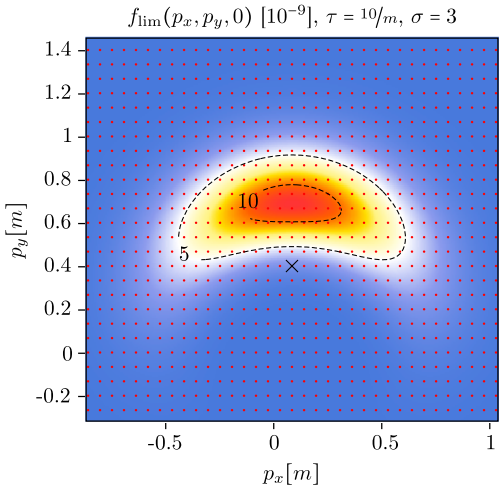

FIG. 5 (color online). Momentum distribution of pairs created by a rotating electric field pulse with $\sigma = 3$ rotation cycles, a pulse duration of $\tau = 10/m$ and a peak field strength $\varepsilon = E_0/E_{\mathrm{cr}} = 0.1$.

It should be stressed that the semiclassical picture cannot cover all aspects of pair production. Though it is useful for understanding the asymptotic momentum distributions for the field configurations studied so far, it finds its limitations in the next example. Even worse, it seems rather useless for understanding the evolution of the distribution function at finite times as discussed below in subsection IV C.

Let us now study larger rotation frequency, i. e. a larger number of rotation cycles σ, while keeping the pulse duration fixed. The case of $\sigma = 6$ is shown in Fig. 6. For increasing σ, we observe that the circular distortion closes into a ring, and another ring can form inside the first

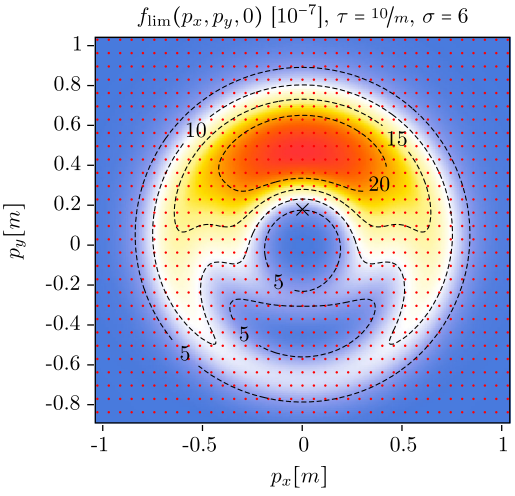

FIG. 6 (color online). Momentum distribution of pairs created by a rotating electric field pulse with $\sigma = 6$ rotation cycles, a pulse duration of $\tau = 10/m$ and a peak field strength $\varepsilon = E_0/E_{\mathrm{cr}} = 0.1$.

ring, while the momentum space radius of the outer ring grows.

An understanding of this pattern requires to go beyond the quasiclassical particle picture. In fact, the production process is a quantum mechanical process, implying that the produced particles also carry phase information. In particular, the right-moving particles with positive p_x carry a generically different phase than the left-moving particles with negative p_x for the case of a circularly distorted distribution. For larger σ, these ends of the distribution now meet again in momentum space to form a ring. Since this corresponds to a sum of quantum mechanical wave functions with different phases, we expect to see an interference pattern. This is in fact, what we observe along the negative p_y axis at $p_x = 0$.

We can even go one step further and try to relate the maxima of the ring-shaped interference pattern to the excess energy in a multiphoton pair production process: a multiphoton picture for pair production implies that a merger of n photons of frequency Ω distributed over the electron and positron should give an average excess energy of $p = 1/2\sqrt{(n\Omega)^2 - 4m^2}$ per particle. In fact, for example the outer ring in Fig. 6 has a radius of about $p \simeq 0.66m$ which approximately matches with the current pulse parameters for $n = 4$, $p = \sqrt{(2 \cdot 0.6m)^2 - m^2}$. Slight deviations to this simple picture can be interpreted as signatures of the effective mass of the fermion in the strong-field environment [56].

As can be anticipated, the particle distribution becomes isotropic for very high rotation frequencies, because the field rotates many times under the envelope and does not change much from one cycle to another. We observe this behavior already for $\sigma = 10$ for our pulse parameters, as is depicted in Fig. 7.

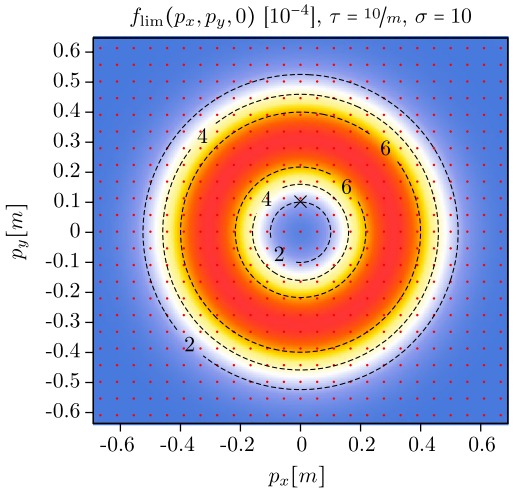

FIG. 7 (color online). Momentum distribution of pairs created by a rotating electric field pulse with $\sigma = 10$ rotation cycles, a pulse duration of $\tau = 10/m$ and a peak field strength $\varepsilon = E_0/E_{\mathrm{cr}} = 0.1$.

We also observe that all distributions exhibit a mirror symmetry in momentum space with respect to $q_x = 0$. This is already the case for the Sauter pulse and holds still true for the more involved momentum distributions generated from the rotating electric field. At first sight, this looks surprising, because the electric field at the instant of reaching its peak field strength points into the x direction, seemingly representing an asymmetry in this direction. As shown in [54] for the case of the Sauter pulse, the observed symmetry can be related to the time reversal symmetry of the x component of the electric field. The very same arguments go through for our choice of the rotating electric

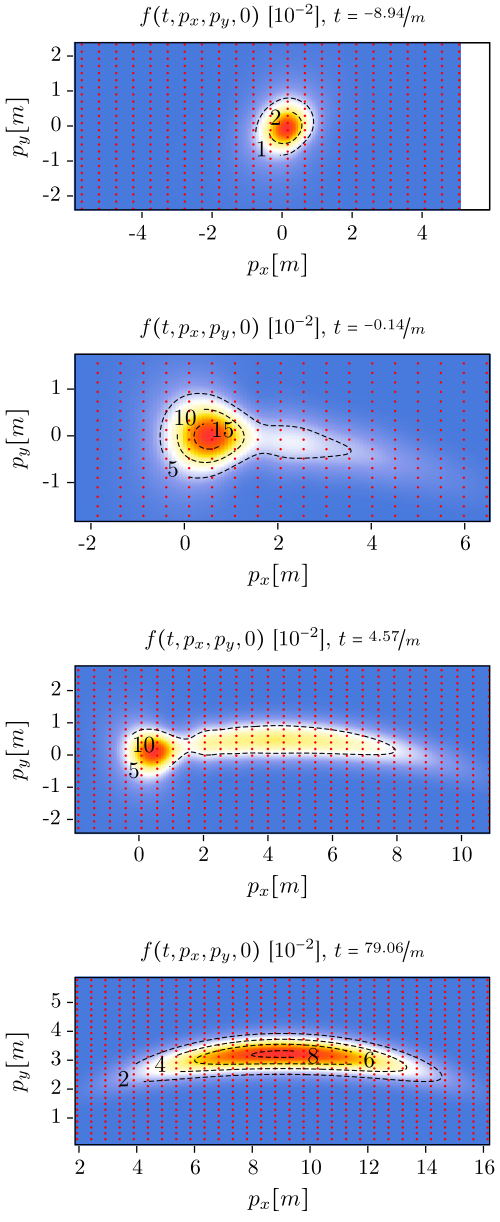

FIG. 8 (color online). Time evolution of the distribution function for a strong field pulse with $\varepsilon = 1$ and pulse duration $\tau = 10/m$ at $\sigma = 1/2$ rotation cycles.

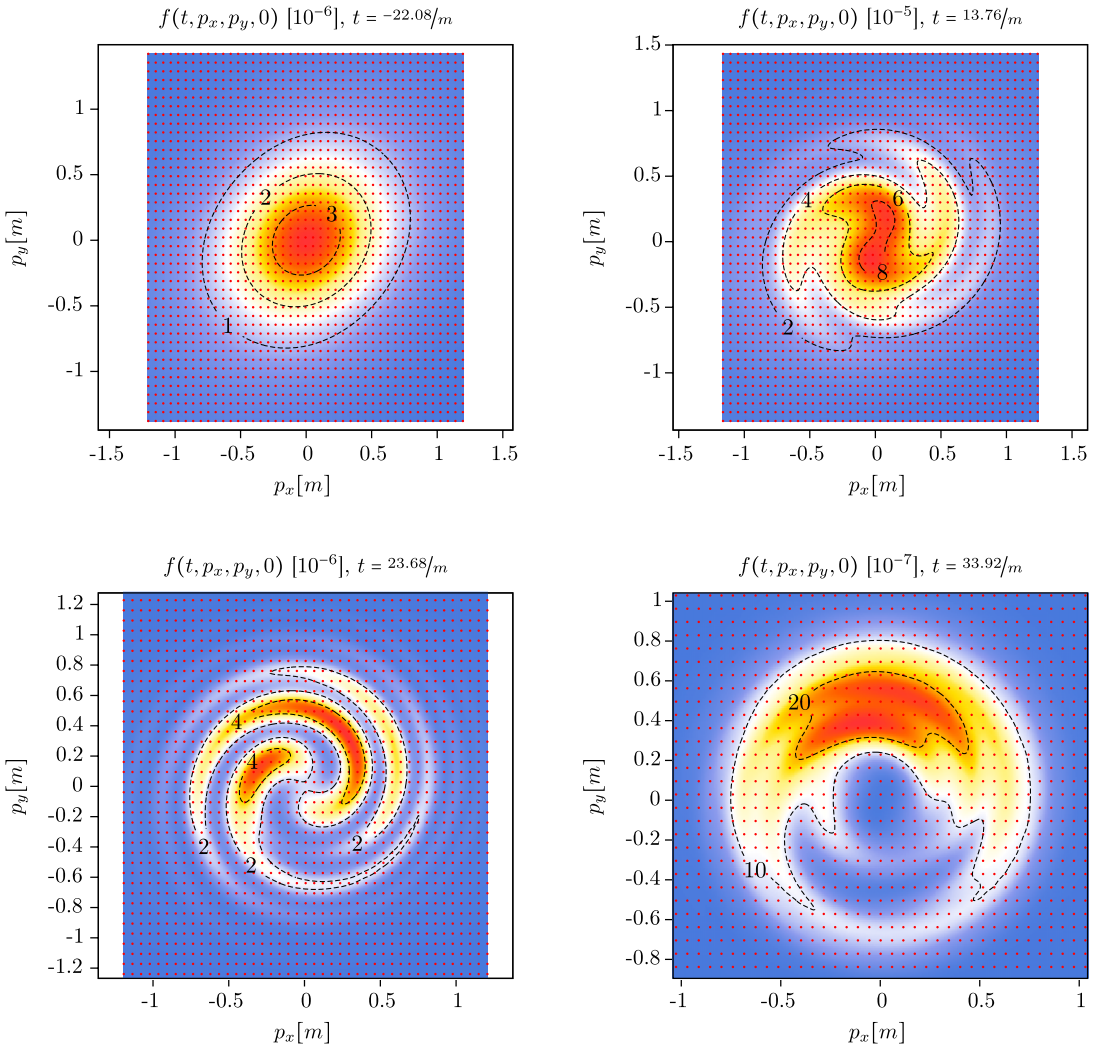

FIG. 9 (color online). Time evolution of the distribution function leading to the momentum distribution shown in Fig. 6 resulting from a rotating pulse with $\varepsilon = 1/10$, $\tau = 10/m$ and $\sigma = 6$.

field and hence imply the same symmetry property for the momentum space distribution.

From a phenomenological viewpoint, this leads us to an important conclusion: for rotating electric field pulses with rotation cycles on the order of $\sigma \gtrsim \mathcal{O}(1)$, we observe a characteristic particle distribution in momentum space starting from moderately circularly distorted distributions as in Fig. 5 to highly asymmetric circular distributions as in Fig. 6. Most importantly, the dominant peak of the distribution does not point into the direction of the peak electric field (x direction in the present example), but orthogonally to this direction within the plane of rotation. We believe that this circular asymmetry can serve as a characteristic signature for pair production.

We should mention that for increasing pulse durations two numerical problems arise. The first problem is an increase of the required computation time per trajectory. This is due to oscillations of some components of the function $\mathbb{w}_9$ which demand for the number of integration steps being at least proportional to the pulse duration. As a second problem, the momentum distribution develops filigree structures that require a large number of lattice points. Both problems increase the necessary computation time but can still be compensated by using faster computers.

C. Time evolution

As emphasized above, the one-particle distribution function can be interpreted as a phase space particle density only at asymptotic times $t \to \infty$. At intermediate times, it has no physical meaning in terms of directly accessible observables. Still, from Eq. (7), the distribution function may give some intuition on a kind of normalized energy density that may be attributed to virtual excitations of the electron-positron field. This viewpoint is also suggested

within quantum kinetic theory where the Vlasov equation for the distribution function is derived with the aid of a Bogoliubov transformation. The latter connects vacuum Fock space ladder operators with quasiparticle creation and annihilation operators at intermediate times. Only for asymptotic times when the field has subsided, these quasiparticle operators can be uniquely connected with a particle Fock space. Nonetheless the time evolution of the function f continuously connects the asymptotic regimes and hence carries relevant information that is worthwhile to be studied. It should, however, be kept in mind that virtual and real particle information is intertwined at intermediate times. In the strong field regime, this interlocking seems less severe such that the time evolution of the distribution function can be interpreted straightforwardly. As an example, we consider a pulse with field strength $E_0 = E_{\rm cr}$, i. e., $\varepsilon = 1$, pulse duration $\tau = 10/m$ and $\sigma = 1/2$ rotation cycles. A series of snapshots at intermediate times shortly before, during and after the pulse are shown in Fig. 8. When the pulse starts to set in (top panel, $t = -8.94/m$), virtual field excitations can be observed near zero momentum $\vec{p} = 0$. Whereas this zero-momentum peak is further enhanced during the pulse evolution, some part of these excitations is accelerated along the direction of the field (predominantly $\sim x$ direction). The distribution develops a tail along the corresponding momentum direction that acquires a slight circular distortion due to the field rotation, cf. 2nd and 3rd panel at $t = -0.14/m$ and $t = 4.57/m$, respectively. Towards asymptotic times, the previously dominant zero momentum peak of virtual excitations vanishes again, and the momentum-space distribution of outgoing real particles forms with the characteristic circular distortion visible in the lowest panel at $t = 79.06/m$. (Apart from this distortion, the result is very similar to that for the Sauter pulse for $\sigma = 0$.)

It is interesting to note that the aforementioned mirror symmetry of the asymptotic distribution about the $q_x = 0$ axis is not present at intermediate times. This can be explained with the fact that the x component of the field is not time reversal symmetric if the evolution is cut off at some finite time t. Only the global field features the required properties.

The separation between virtual excitations and real pairs becomes less obvious at weaker field strengths. Quantum mechanical phase and interference effects become more important in this regime. This is illustrated in Fig. 9 for a field strength of $\varepsilon = E_0/E_{\rm cr} = 0.1$ and a pulse duration of $\tau = 10/m$ with $\sigma = 6$ rotation cycles. There is no clear separation between a virtual excitation peak or a real particle tail neither in height nor in momentum space. In addition, the rotation of the field appears to induce stronger interference effects. Only when the pulse has almost faded away the virtual excitations relax and the circular distribution pattern starts to form yielding the asymptotic result of Fig. 6.

V. CONCLUSION AND OUTLOOK

We have investigated Schwinger pair production in rotating time-dependent electric fields for the first time using the DHW formalism for a numerical computation of the Wigner function. With this method, we have access to particle or antiparticle distributions in momentum space, the total particle yield as well as the whole time evolution of the production process.

We find that rotation generically enhances pair production in comparison with a linearly polarized field pulse. This is heuristically clear since rotation introduces more Fourier modes that lead to a pair production increase similar to multiphoton effects for linear oscillating pulses. We have corroborated this interpretation by introducing an effective Keldysh parameter that accounts for the time scales of both the pulse as well as of the rotation. For a sufficiently large number of rotation cycles, the data for the total particle yield falls on a universal curve. This universal curve can be parametrized by a multiphoton description in terms of the effective Keldysh parameter.

Even more interesting features can be read off from the momentum space distribution of the produced particles. The rotating field leaves several characteristic imprints on the distribution depending on the number of rotation cycles. Rotation can in particular be read off from the shape of the distribution, from the (partly counterintuitive) location of the peak, and from resulting interference patterns. Depending on the parameter regime, some of these features can be understood in a simple quasiclassical picture or in terms of multiphoton physics, whereas an understanding of the interferences requires a full quantitative treatment of the quantum mechanical phase information.

From a technical viewpoint, we have shown that the DHW equations can be solved with the method of characteristics for general spatially homogeneous time-dependent electric fields. In particular, a commonly made restriction to unidirectional fields is not necessary. For this generalized class of fields, the PDE system of DHW equations can be mapped onto an ODE system similar to quantum kinetic theory.

In view of our original motivation arising from QED cascades, we believe that the characteristic momentum space patterns of the distribution function can serve as a decisive fingerprint of Schwinger pair production, provided the QED successive cascade preserves a remnant of this pattern in the final state distributions of either electrons, positrons or photons. If so, a QED cascade seeded by the pair production process studied in this work could be quantitatively distinguished from a more mundanely sourced cascade stimulated by isotropic vacuum impurities. To answer this question, our results for the particle distribution should be used as initial conditions of a QED cascade calculation.

ACKNOWLEDGMENTS

We are grateful to R. Alkofer, J. Borchardt, C. Kohlfürst, S. Krause, H. Ruhl, D. Schinkel and N. Seegert for interesting and enlightening discussions. We acknowledge support by the DFG under Grants No. Gi 328/5-2 (Heisenberg program), No. GRK 1523/2, and No. SFB-TR18.

APPENDIX: NUMERICAL DETAILS

Numerical solutions of Eq. (22) have been computed using *Wolfram Mathematica*. It's built-in numerical differential equation solver, `NDSolve` uses various solution methods in combination with adaptive step size and error estimation techniques. The main method used for ordinary differential equations is `LSODA` which is part of the `ODEPACK` package [57]. It dynamically switches between nonstiff (Adams) and stiff (backward differentiation formula) methods.

In order to achieve the required accuracy it is important to set the error bounds for the adaptive step size. The `NDSolve` method of *Mathematica* accepts two parameters `AccuracyGoal` and `PrecisionGoal`. If a function f is calculated from some ODE the resulting upper bound for the estimate integration error is

$$\Delta_{\max} = 10^{-\texttt{AccuracyGoal}} + |f| 10^{-\texttt{PrecisionGoal}}, \quad \text{(A1)}$$

where $10^{-\texttt{AccuracyGoal}}$ is a tolerable absolute error and $10^{-\texttt{PrecisionGoal}}$ is a tolerable relative error. The value of the actual function f ranges over many orders of magnitude as shown in Fig. 10 for an example trajectory and a typical set of parameters. The result of physical interest is the comparatively small function value at asymptotically large times. As the peak value near $t = 0$ exceeds the asymptotic result by many orders of magnitude, relative errors are generically unacceptable, because the error bound could then easily exceed the final physical value during time steps near the peak value. We hence accept only an absolute error by setting `PrecisionGoal` to the special value `Infinity`.

Also the decay of the transient oscillations caused by actually switching on the field at a finite (large negative) time can be seen in Fig. 10.

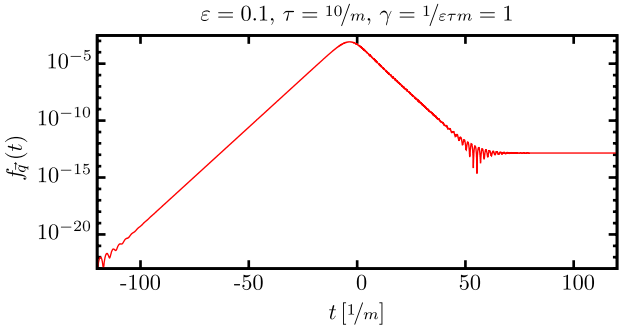

FIG. 10 (color online). Distribution function f along an example trajectory.

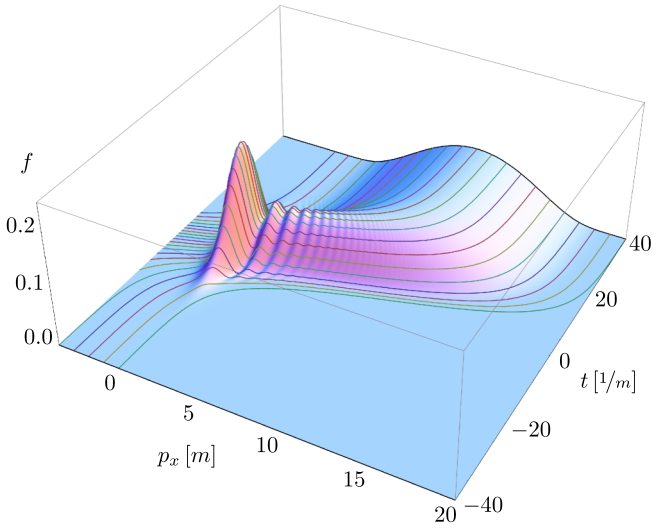

FIG. 11 (color online). Comparison between the analytic solution for the Sauter pulse ($\Omega = 0$) (full surface) and the numerical solution along some (colored) trajectories.

As shown in Fig. 11, the employed methods can reproduce analytical solutions quite well. In this plot, the exact solution for the Sauter pulse with $\Omega = 0$ and $\tau = 10/m$ and $\varepsilon = 1$ shown as a surface plot is superposed by the numerical solutions along a set of characteristics (colored line plots). Both solutions agree very well even in the strongly oscillatory regime near the time of peak field strength $t = 0$.

[1] F. Sauter, Z. Phys. **69**, 742 (1931).
[2] W. Heisenberg and H. Euler, Z. Phys. **98**, 714 (1936).
[3] J. S. Schwinger, Phys. Rev. **82**, 664 (1951).
[4] A. Ringwald, Phys. Lett. B **510**, 107 (2001).
[5] R. Alkofer, M. B. Hecht, C. D. Roberts, S. M. Schmidt, and D. V. Vinnik, Phys. Rev. Lett. **87**, 193902 (2001).
[6] R. Schutzhold, H. Gies, and G. Dunne, Phys. Rev. Lett. **101**, 130404 (2008).
[7] M. Ruf, G. R. Mocken, C. Muller, K. Z. Hatsagortsyan, and C. H. Keitel, Phys. Rev. Lett. **102**, 080402 (2009).
[8] A. Di Piazza, E. Lotstedt, A. I. Milstein, and C. H. Keitel, Phys. Rev. Lett. **103**, 170403 (2009).

[9] G. V. Dunne, H. Gies, and R. Schutzhold, Phys. Rev. D **80**, 111301 (2009).
[10] A. Monin and M. B. Voloshin, Phys. Rev. D **81**, 025001 (2010).
[11] V. N. Baier and V. M. Katkov, Phys. Lett. A **374**, 2201 (2010).
[12] T. Heinzl, A. Ilderton, and M. Marklund, Phys. Lett. B **692**, 250 (2010).
[13] S. S. Bulanov, V. D. Mur, N. B. Narozhny, J. Nees, and V. S. Popov, Phys. Rev. Lett. **104**, 220404 (2010).
[14] A. Gonoskov, I. Gonoskov, C. Harvey, A. Ilderton, A. Kim, M. Marklund, G. Mourou, and A. M. Sergeev, Phys. Rev. Lett. **111**, 060404 (2013).
[15] C. Muller, A. Di Piazza, A. Shahbaz, T. Burvenich, J. Evers, K. Hatsagortsyan, and C. Keitel, Laser Phys. **18**, 175 (2008).
[16] C. Muller, K. Z. Hatsagortsyan, M. Ruf, S. J. Muller, H. G. Hetzheim, M. C. Kohler, and C. H. Keitel, Laser Phys. **19**, 1743 (2009).
[17] A. Di Piazza, E. Lotstedt, A. I. Milstein, and C. H. Keitel, Phys. Rev. A **81**, 062122 (2010).
[18] A. Di Piazza, A. I. Milstein, and C. Muller, Phys. Rev. A **82**, 062110 (2010).
[19] A. R. Bell and J. G. Kirk, Phys. Rev. Lett. **101**, 200403 (2008).
[20] J. G. Kirk, A. R. Bell, and I. Arka, Plasma Phys. Controlled Fusion **51**, 085008 (2009).
[21] A. M. Fedotov, N. B. Narozhny, G. Mourou, and G. Korn, Phys. Rev. Lett. **105**, 080402 (2010).
[22] S. S. Bulanov, T. Z. Esirkepov, A. G. R. Thomas, J. K. Koga, and S. V. Bulanov, Phys. Rev. Lett. **105**, 220407 (2010).
[23] N. V. Elkina, A. M. Fedotov, I. Y. Kostyukov, M. V. Legkov, N. B. Narozhny, E. N. Nerush, and H. Ruhl, Phys. Rev. ST Accel. Beams **14**, 054401 (2011).
[24] E. N. Nerush, I. Y. Kostyukov, A. M. Fedotov, N. B. Narozhny, N. V. Elkina, and H. Ruhl, Phys. Rev. Lett. **106**, 035001 (2011); **106**, 109902(E) (2011).
[25] E. N. Nerush, V. F. Bashmakov, and I. Y. Kostyukov, arXiv:1105.3981.
[26] B. King, N. Elkina, and H. Ruhl, Phys. Rev. A **87**, 042117 (2013).
[27] S. S. Bulanov, C. B. Schroeder, E. Esarey, and W. P. Leemans, Phys. Rev. A **87**, 062110 (2013).
[28] V. F. Bashmakov, E. N. Nerush, I. Y. Kostyukov, A. M. Fedotov, and N. B. Narozhny, arXiv:1310.4077.
[29] S. P. Kim and D. N. Page, Phys. Rev. D **65**, 105002 (2002).
[30] H. Gies and K. Klingmuller, Phys. Rev. D **72**, 065001 (2005).
[31] G. V. Dunne and C. Schubert, Phys. Rev. D **72**, 105004 (2005);
[32] G. V. Dunne, Q.-h. Wang, H. Gies, and C. Schubert, Phys. Rev. D **73**, 065028 (2006).
[33] E. Brezin and C. Itzykson, Phys. Rev. D **2**, 1191 (1970).
[34] N. B. Narozhnyi and A. I. Nikishov, Yad. Fiz. **11**, 1072 (1970) [Sov. J. Nucl. Phys. **11**, 596 (1970)].
[35] V. S. Popov, J. Exp. Theor. Phys. **34**, 709 (1972).
[36] V. S. Popov and M. S. Marinov, Yad. Fiz. **16**, 809 (1972).
[37] S. P. Gavrilov and D. M. Gitman, Phys. Rev. D **53**, 7162 (1996).
[38] G. V. Dunne and T. Hall, Phys. Rev. D **58**, 105022 (1998).
[39] D. D. Dietrich, Phys. Rev. D **68**, 105005 (2003).
[40] A. D. Piazza, Phys. Rev. D **70**, 053013 (2004).
[41] G. V. Dunne and Q.-h. Wang, Phys. Rev. D **74**, 065015 (2006).
[42] D. D. Dietrich and G. V. Dunne, J. Phys. A **40**, F825 (2007).
[43] F. Hebenstreit, R. Alkofer, and H. Gies, Phys. Rev. Lett. **107**, 180403 (2011).
[44] I. Bialynicki-Birula, P. Gornicki, and J. Rafelski, Phys. Rev. D **44**, 1825 (1991).
[45] F. Hebenstreit, R. Alkofer, and H. Gies, Phys. Rev. D **82**, 105026 (2010).
[46] F. Hebenstreit, arXiv:1106.5965.
[47] S. A. Smolyansky, G. Ropke, S. M. Schmidt, D. Blaschke, V. D. Toneev, and A. V. Prozorkevich, arXiv:hep-ph/9712377.
[48] Y. Kluger, E. Mottola, and J. M. Eisenberg, Phys. Rev. D **58**, 125015 (1998).
[49] S. M. Schmidt, D. Blaschke, G. Ropke, S. A. Smolyansky, A. V. Prozorkevich, and V. D. Toneev, Int. J. Mod. Phys. E **07**, 709 (1998).
[50] J. C. R. Bloch, V. A. Mizerny, A. V. Prozorkevich, C. D. Roberts, S. M. Schmidt, S. A. Smolyansky, and D. V. Vinnik, Phys. Rev. D **60**, 116011 (1999).
[51] F. Hebenstreit, R. Alkofer, and H. Gies, Phys. Rev. D **78**, 061701 (2008).
[52] F. Hebenstreit, R. Alkofer, G. V. Dunne, and H. Gies, Phys. Rev. Lett. **102**, 150404 (2009); arXiv:0910.4457.
[53] C. K. Dumlu and G. V. Dunne, Phys. Rev. Lett. **104**, 250402 (2010).
[54] C. K. Dumlu and G. V. Dunne, Phys. Rev. D **83**, 065028 (2011).
[55] T. Nousch, D. Seipt, B. Kampfer, and A. I. Titov, Phys. Lett. B **715**, 246 (2012).
[56] C. Kohlfürst, H. Gies, and R. Alkofer, Phys. Rev. Lett. **112**, 050402 (2014).
[57] A. C. Hindmarsh, Scientific Computing **1**, 55 (1983).